SUPPLEMENTARY INFORMATION

Scalable One-pot Bacteria-templating Synthesis Route toward Hierarchical, Porous-Co_3O_4 Superstructures for Supercapacitor Electrodes

Hyun-Woo Shim[1], Ah-Hyeon Lim[1], Jae-Chan Kim[1], Eunjin Jang[2], Seung-Deok Seo[1], Gwang-Hee Lee[1], T. Doohun Kim[2], and Dong-Wan Kim[1]*

[1]Department of Materials Science and Engineering, Ajou University, Suwon, 443-749, Korea.

[2]Department of Molecular Science and Technology, Graduate School of Interdisciplinary Programs, Ajou University, Suwon, 443-749, Korea.

* To whom correspondence should be addressed. E-mail: dwkim@ajou.ac.kr; Fax: +82 31 219 3248; Tel: +82 31 219 2468

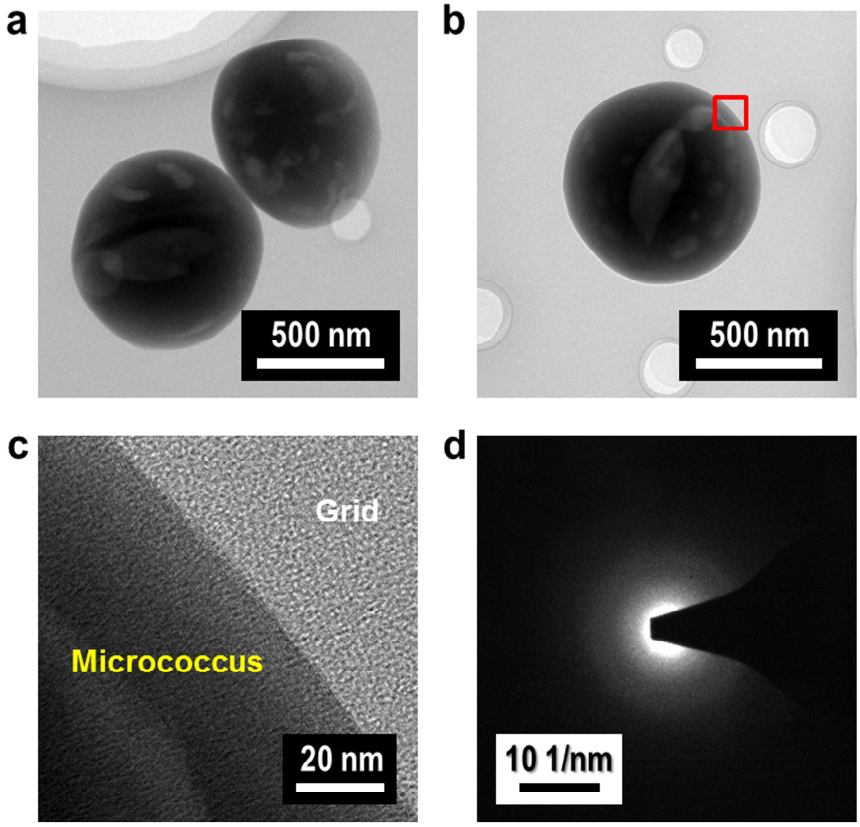

Figure S1. TEM characterization of the original *Micrococcus* cell. a, **b**, Low-magnification TEM image (**a**) and an individual TEM micrograph (**b**) showing spherical shapes approximately 800 nm to 1 µm in diameter. **c**, HR-TEM image taken from the region indicated by the open-square in (**b**). The image shows that the surface of the *Micrococcus* cell is smooth. **d**, The SAED pattern for a pure bacterial sample, showing an amorphous nature.

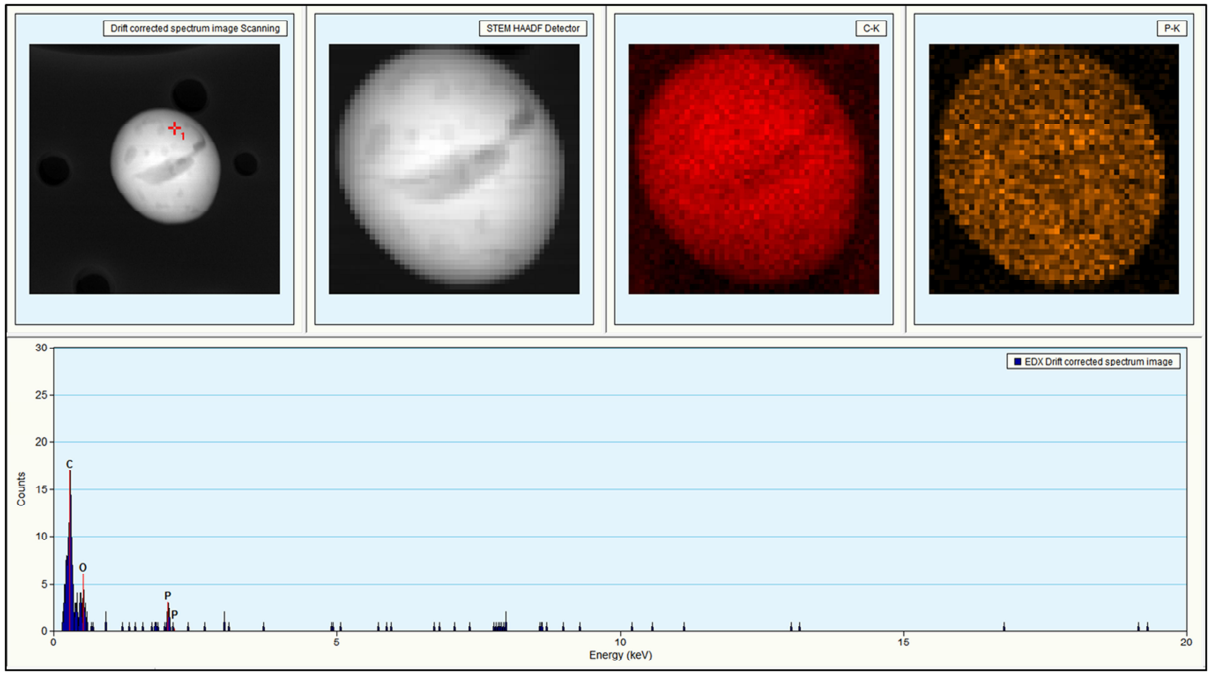

Figure S2. TEM characterization of the original *Micrococcus* cell. A high-angle annular dark-field (HAADF) scanning transmission electron microscope (STEM) image and the corresponding EDS analysis/elemental mapping (carbon and phosphorous) for an individual *Micrococcus* cell. The quantitative EDS analysis was performed at the position marked as "1" in the STEM image.

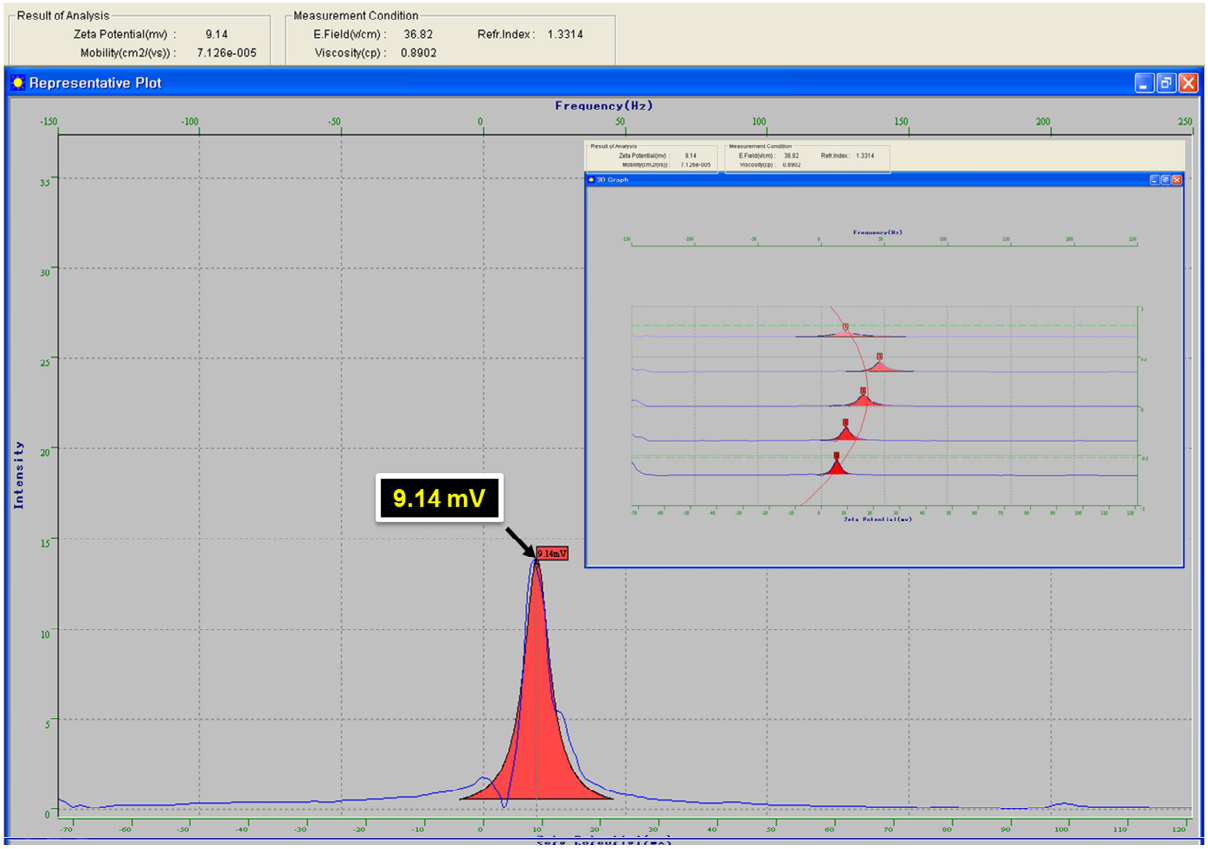

Figure S3. Zeta-potential (ζ) measurement of the obtained product (the bacteria-supported, hierarchical, porous-Co_3O_4 powder dispersed in distilled water) after the complete 12-h reaction. The ~9-mV zeta-potential is the average of 5 measured zeta-potentials (inset) and suggests that the sample has no more negative charge, implying the existence of cobalt oxides combined with bacterial templates after the 12-h reaction.

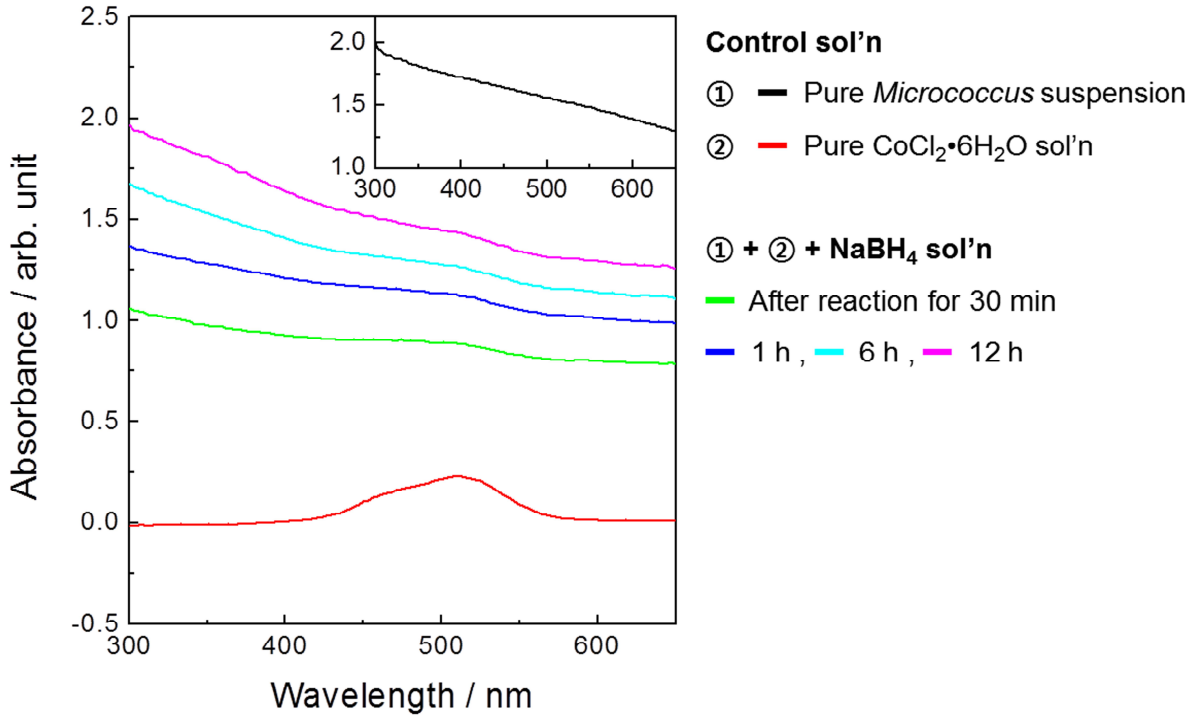

Figure S4. UV-visible characterization. UV-visible absorption spectra of the solutions obtained at each synthetic stage. The inset shows the UV-visible absorption spectrum of a pure *Micrococcus* suspension.

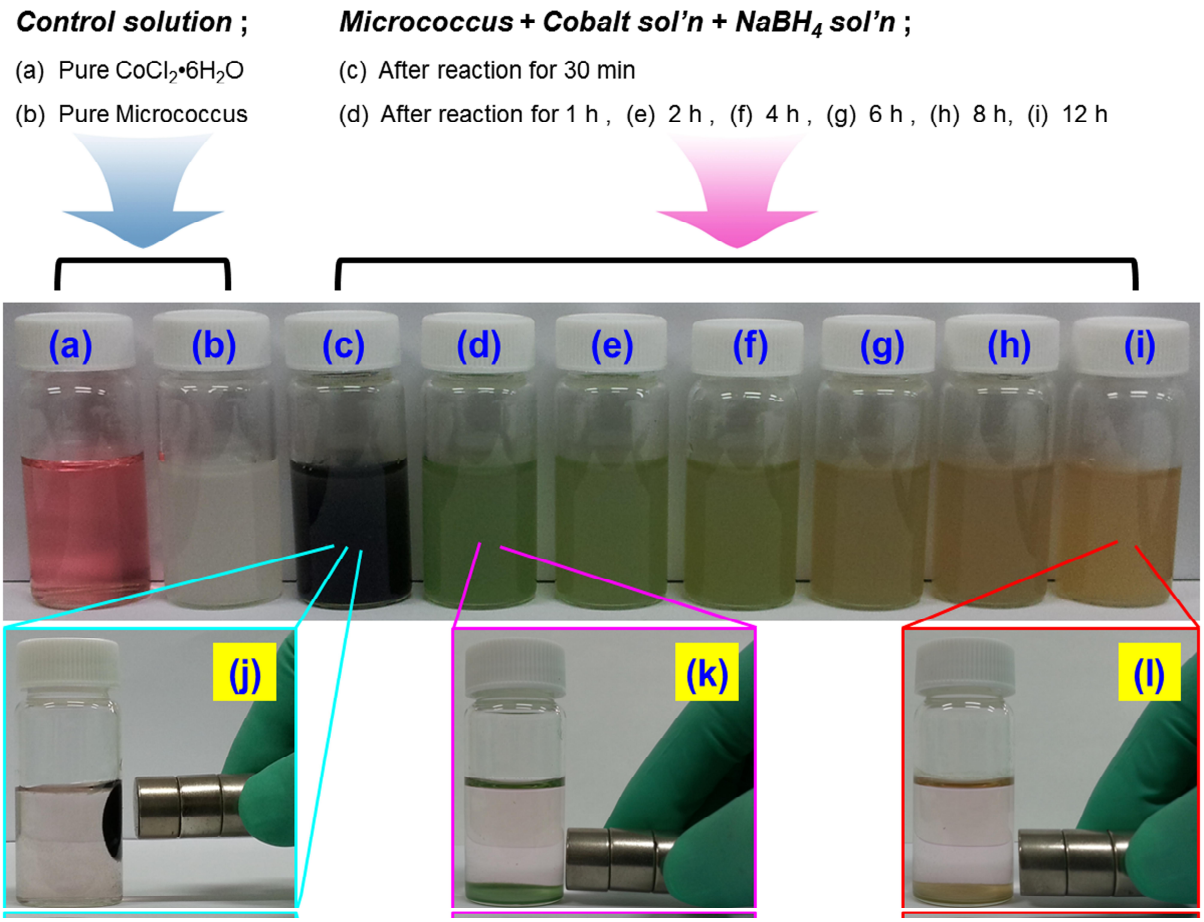

Figure S5. Representative digital photograph of the samples prepared at various stages of synthesis. a, **b**, The cobalt precursor solution used in this work (**a**) and the pure *Micrococcus* suspension (**b**) dispersed in distilled water. **c-i**, The final mixture and the associated changes in color obtained by fabricating the hierarchical, porous-Co_3O_4/bacteria structures for various reaction times. **j-l**, The photographs show the magnetic properties of the precipitates corresponding with reaction times of 30 min (**j**), 1 h (**k**), and 12 h (**l**).

Pore analysis by the BJH plot

Porous nature of the RT-Co_3O_4 microspheres is further supported by the Barrett-Joyner-Halenda (BJH) pore size distribution plot, which clearly shows that the pores are in the micro/mesopore region and exhibit multimodal pore size distribution (see inset of Fig. 2f). According to the International Union of Pure and Applied Chemistry (IUPAC) classification, the observed hysteresis loop is ascribed as a "Type IV" loop, indicating the existence of abundant 2–50-nm-diameter pores. It is noteworthy that a distinct hysteresis loop is shown in the *ca.* 0.3–0.95 p/p^0 range, which suggests that the multimodal, hierarchical porosity (*i.e.*, mesopores together with macropores)[R1] of the RT-Co_3O_4 microspheres should be mainly caused by the "cavity" among the assembled Co_3O_4 nanoparticles and the "void" of neighboring 3D-architectures. The average pore diameter of the RT-Co_3O_4 microspheres was calculated as *ca.* 7.7 nm from the BJH method and the adsorption branch of the isotherm, and the pore volume was quantitatively summarized as 0.26 $cm^3\ g^{-1}$. More importantly, the RT-Co_3O_4 microspheres exhibited a large BET specific surface area of *ca.* 149 $m^2\ g^{-1}$. The uptake of N_2 exhibited at the higher relative pressure ($p/p^0 > 0.9$) in the BET isotherm demonstrates the existence of macropores in the microspheres[R1, R2]. The uptake of N_2 exhibited in the macropore region is considerably lower than that exhibited in the mesopore region of the BET isotherm for the RT-Co_3O_4 microspheres. Therefore, the contribution of mesopores to the total surface area and pore volume of the microspheres is significantly larger than that of the macropores. More importantly, the large BET specific surface area and porous structure of the RT-Co_3O_4 microspheres facilitate fast penetration of the electrolyte and provide a great amount of contact area between the electrolyte and the electroactive surface of the microspheres, thereby providing efficient transport of electrons and ions throughout the electrode and leading to enhanced electrochemical performance for energy storage.

References

R1. Xiao, Y. *et al.* 3D hierarchical Co_3O_4 twin-spheres with an urchin-like structure: large-scale synthesis, multistep-splitting growth, and electrochemical pseudocapacitors. *Adv. Funct. Mater.* **22,** 4052-4059 (2012).

R2. Rouquerol, F., Rouquerol, J. & Sing, K. S. W. *Adsorption by Powders and Porous Solids: Principles, Methodology and Applications* (Academic Press, 1999).

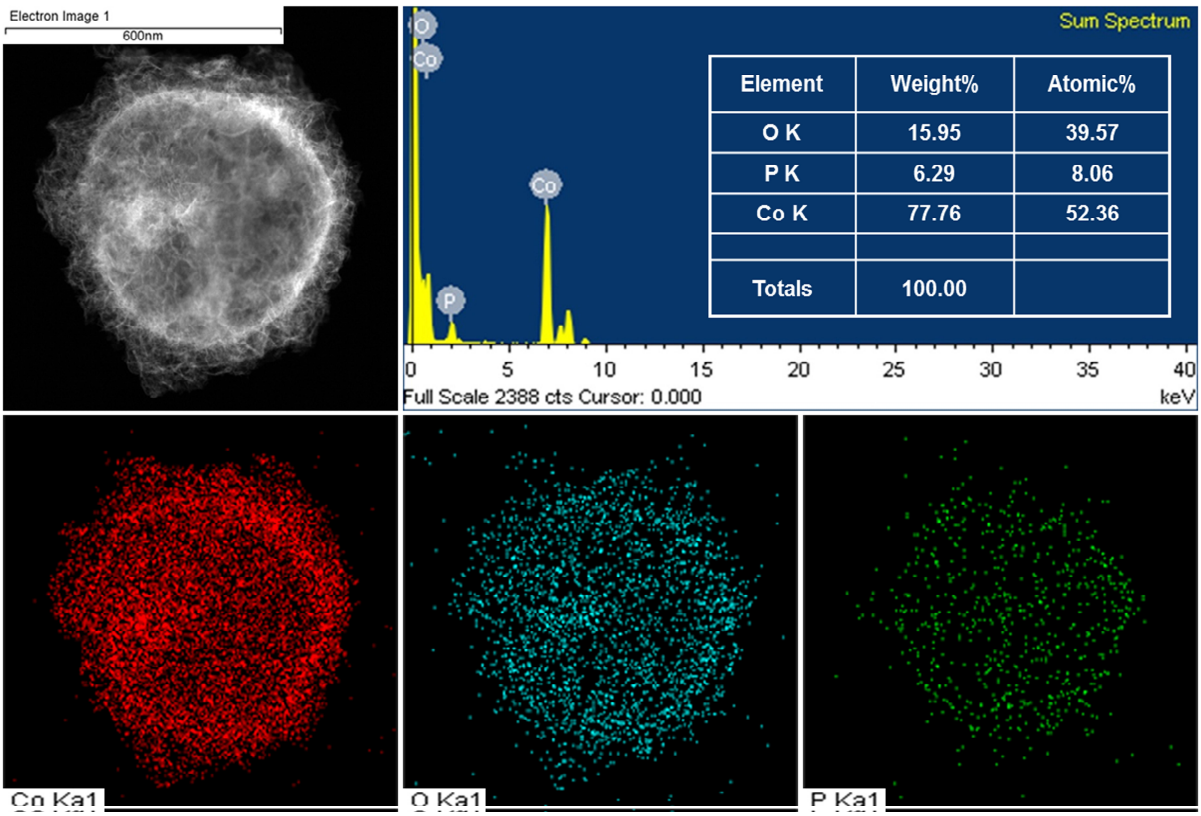

Figure S6. TEM characterization of the bacteria-supported, hierarchical, porous-Co_3O_4 microsphere. The HAADF STEM image and the EDS analysis/elemental mappings (cobalt, oxygen, and phosphorous) for an individual structure. The inset in the quantitative EDS analysis for each atomic percent shows the precise Co_3O_4 composition.

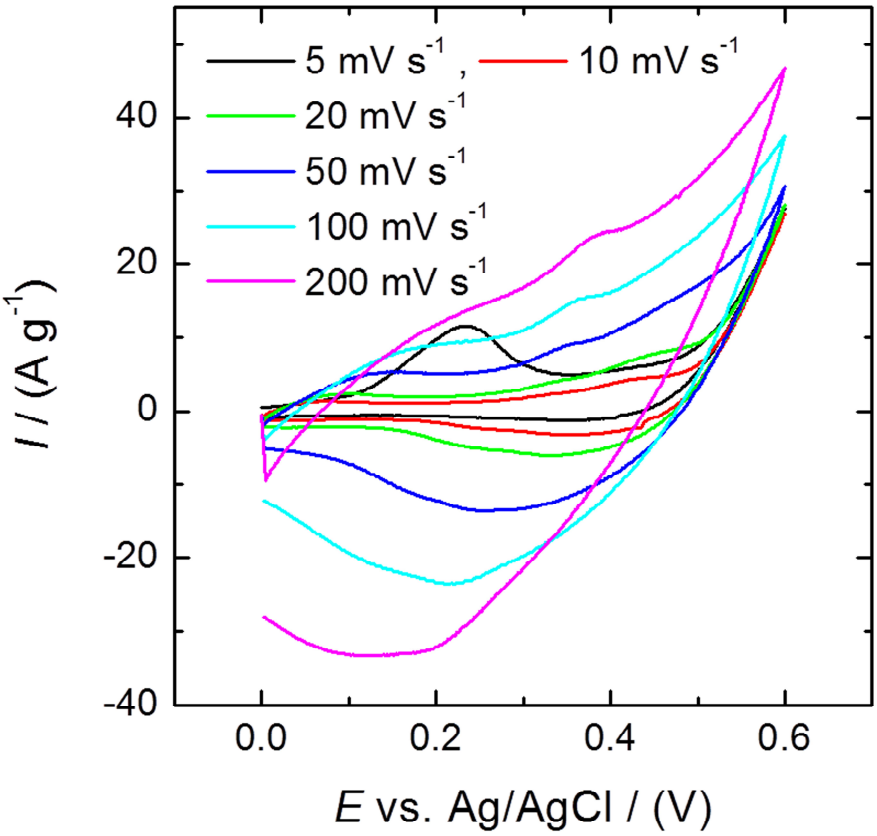

Figure S7. Initial CV profiles for the electrode produced using the bacteria-supported, hierarchical, porous-Co_3O_4 microspheres. The CV profiles were measured between 0 and 0.6 V at scan rates of 5 (black line), 10 (red line), 20 (green line), 50 (blue line), 100 (cyan line), and 200 mV s^{-1} (pink line).

Calculation of the specific capacitance

Following equations are used to derive the specific capacitance (SC), measured in Faradays per gram or per area, from the CVs or galvanostatic cycling profiles (CPs), respectively[20, 21, R3].

$$SC_{cv}\,(F\,g^{-1}) = \frac{Q}{\Delta E \times M} \text{ and} \qquad (1)$$

$$SC_{cp}\,(F\,g^{-1}) = \frac{I \times \Delta t}{\Delta E \times M}\,, \qquad (2)$$

where Q (in C or mA·s) represents the integrated cathodic (or anodic) charge, ΔE (in V) represents the potential window, I (in mA) represents the amount of current applied to the electrode during charging-discharging, Δt (in sec) represents the amount of time elapsed during the discharge, and M (in mg) represents the loading mass of the active materials.

References

20. Conway, B. E. *Electrochemical Supercapacitors: Scientific Fundamentals and Technological Applications* (Kluwer Academic/Plenum Press, 1999).
21. Wang, H. *et al.* Supercapacitive properties of hydrothermally synthesized Co_3O_4 nanostructures. *J. Phys. Chem. C* **115,** 17599-17605 (2011).
R3. Pech, D. *et al.* Ultrahigh-power micrometre-sized supercapacitors based on onion-like carbon. *Nat. Nanotech.* **5,** 651-654 (2010).

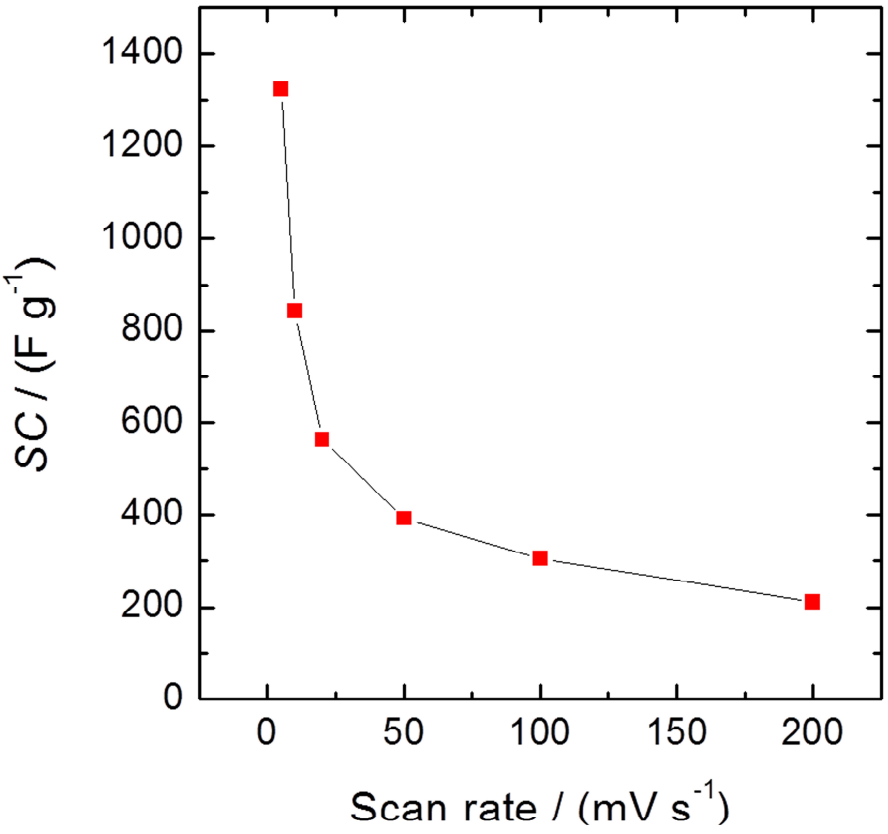

Figure S8. Scan rate dependence of the SC of the electrode produced using bacteria-supported, hierarchical, porous-Co_3O_4 microspheres. The SCs were estimated from the 5th cycle of each CV curve measured at different scan rates. Here, the specific capacitance (C, in F g^{-1}) was calculated using the voltammetric discharge integrated from the cyclic voltammogram over the whole potential range (0.6 V) according to the following equation[20, 21, R3]: $C = Q/(\Delta E \times M)$, where Q represents the charge (in C or mA·s), ΔE represents the potential window (in V), and M represents the loading mass of the active materials (in mg).

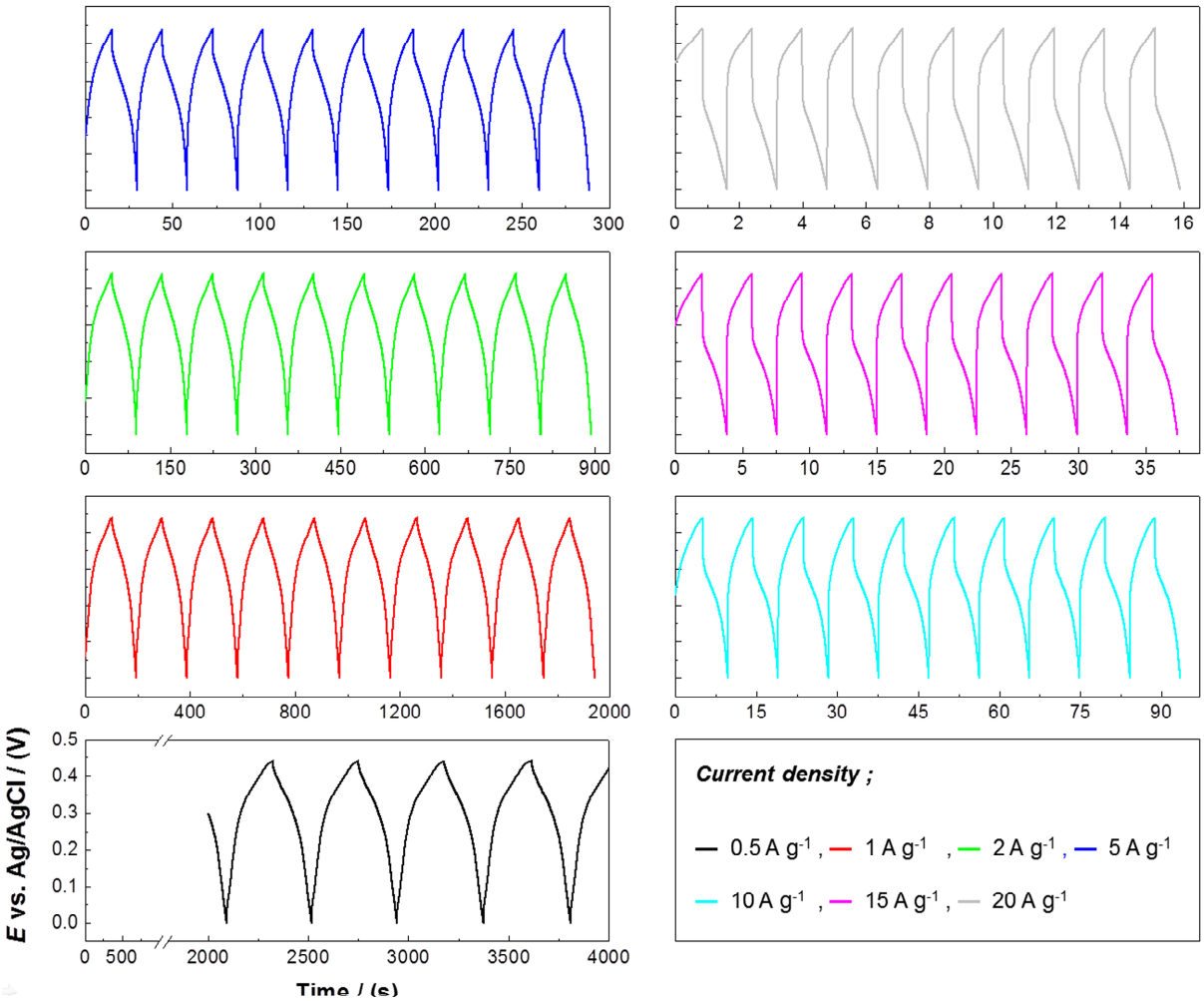

Figure S9. Galvanostatic charge-discharge (voltage *versus* time) curves for the electrode produced using the bacteria-supported, hierarchical porous-Co_3O_4 microspheres measured at seven different current densities from 0.5 to 20 A g^{-1}.

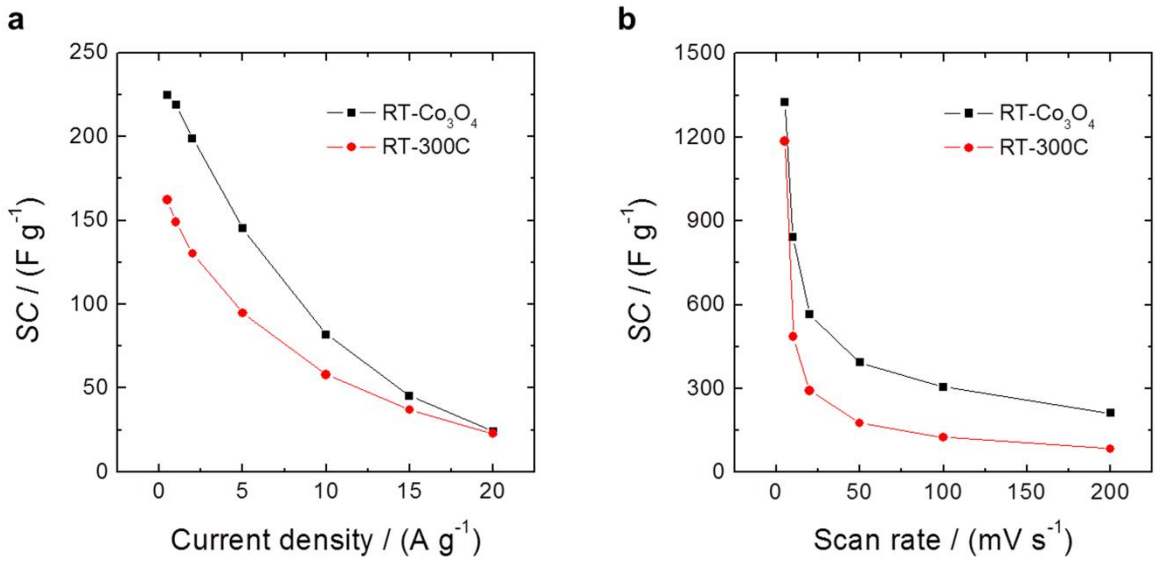

Figure S10. Comparison of the electrochemical evaluations. a, Corresponding specific capacitances (SCs) *vs.* various constant current densities of electrodes. The SCs of all electrodes were estimated from the 5th cycle of charge/discharge curves in the potential window between 0 and 0.44 V (*vs.* Ag/AgCl). **b**, Scan rate dependence of the SCs of the electrodes measured at each scan rate in the potential range of 0 – 0.6 V (*vs.* Ag/AgCl). All electrochemical analyses were carried out under the same conditions: a beaker-type three-electrode system with an aqueous electrolyte solution (3 M KOH) at room temperature.

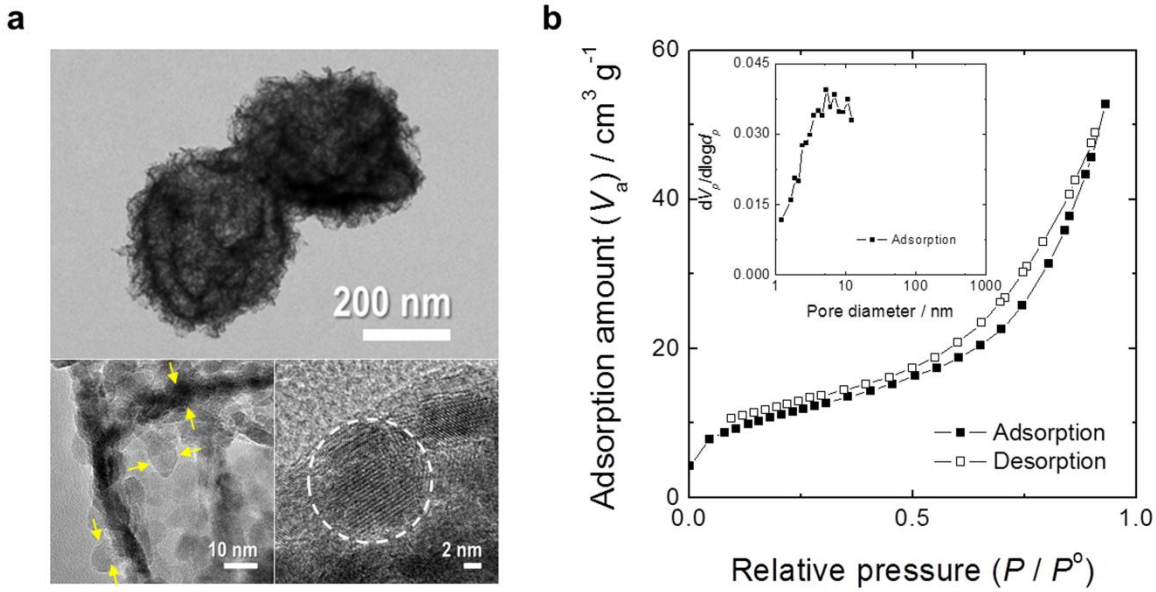

Figure S11. The characterization of RT-300C. a, The representative TEM and HR-TEM images of RT-300C. The arrows and open-circle (dashed line) indicate the bigger Co_3O_4 nanoparticles. **b**, The N_2 adsorption-desorption isotherm and the pore size distribution curve (the inset) of the RT-300C.

Ragone plot

Although it is challenging to accurately compare the performances of all types of supercapacitor electrodes because of numerous variables such as mass loadings of materials, charge-discharge rates, and testing configurations, a rough comparison of the performances can still be made. In this context, we show the Ragone plot (power density *vs.* energy density) for the RT-Co_3O_4-microsphere-based electrode (see Fig. S9). The specific energy (E) and power (P) density derived from galvanostatic charge-discharge tests can be calculated from the following equations[42, R4]:

$$E = \frac{1}{2} C \Delta V^2 \text{ and} \qquad (3)$$

$$P = \frac{E}{\Delta t}, \qquad (4)$$

where E (W h kg^{-1}), C (F g^{-1}), ΔV (V), P (kW kg^{-1}) and Δt (s) represent the specific energy density, specific capacitance, the potential voltage, specific power density, and discharge time during the galvanostatic cycle, respectively. It is impressive that the RT-Co_3O_4-microsphere-based electrode delivered a specific energy density from 21.9 to 3.49 W h kg^{-1} and a specific power density from 117.4 to 4,538 W kg^{-1} as the galvanostatic charge-discharge current density was increased from 0.5 to 20 A g^{-1}.

References

42. Xia, X. *et al.* Freestanding Co_3O_4 nanowire array for high performance supercapacitors. *RSC Adv.* **2,** 1835-1841 (2012).

R4. Yan, J., et al. Khoo, E., Sumboja, A. & Lee, P. S. Facile coating of manganese oxide on tin oxide nanowires with high-performance capacitive behavior. *ACS Nano* **7,** 4247-4255 (2010).

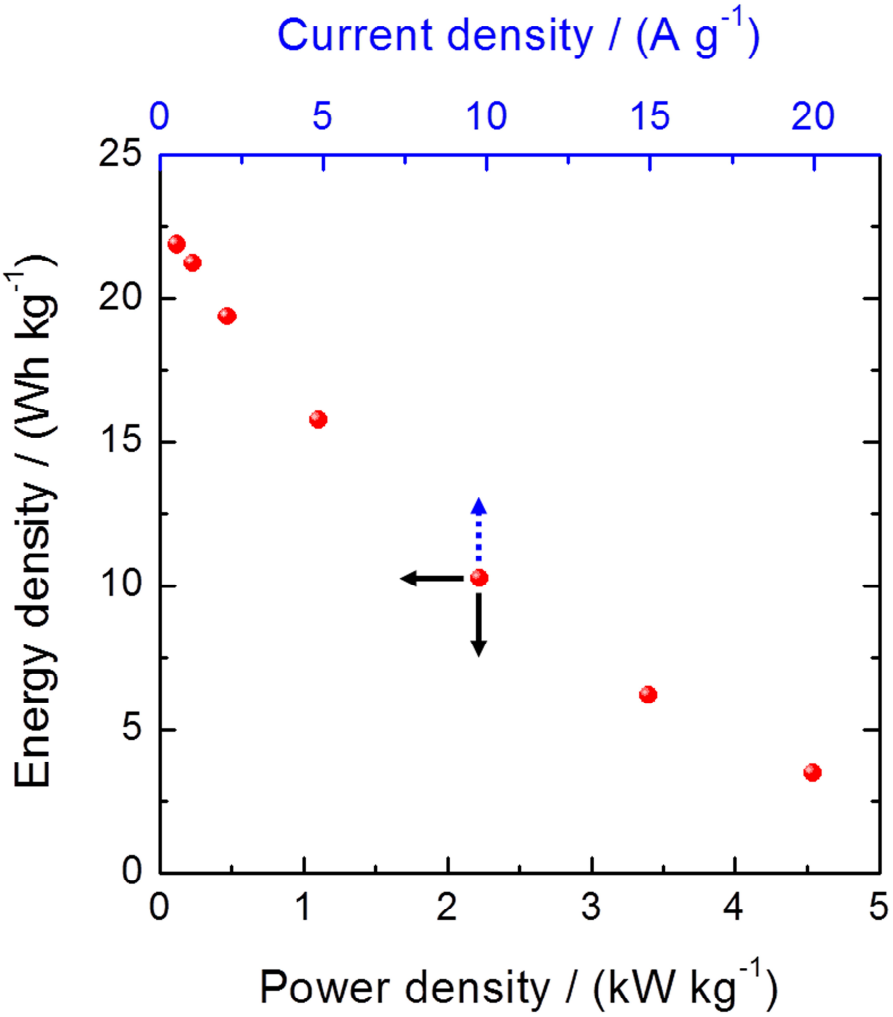

Figure S12. Ragone plot derived from the galvanostatic discharge curves for the electrode produced using the bacteria-supported, hierarchical, porous-Co_3O_4 microspheres measured at seven different current densities from 0.5 to 20 A g^{-1}. Here, the energy density (E) and power density (P) are calculated using the following equations[42, R4]: $E = (C \times \Delta V^2)/2$ and $P = E/\Delta t$, where C (F g^{-1}) represents the specific capacitance of the active material, ΔV (V) represents the cutoff voltage across the electrode, E represents the energy density, and Δt (s) represents the discharge time.

Coulombic efficiency

The Coulombic efficiency (η), which is a measure of completeness of charge/ion transfer during an electrochemical reaction, was also calculated using following equation for each charge-discharge cycle[28, 44]:

$$\eta\ (\%) = \frac{t_D}{t_C} \times 100\ , \qquad (5)$$

where t_D and t_C represent the discharging and charging times in galvanostatic charge-discharge measurements.

References

28. Hou, L. *et al.* Urchin-like Co_3O_4 microspherical hierarchical superstructures constructed by one-dimension nanowires toward electrochemical capacitors. *RSC Adv.* **1,** 1521-1526 (2011).

44. Meher, S. K. & Rao, G. R. Ultralayered Co_3O_4 for high-performance supercapacitor applications. *J. Phys. Chem. C* **115,** 15646-15654 (2011).

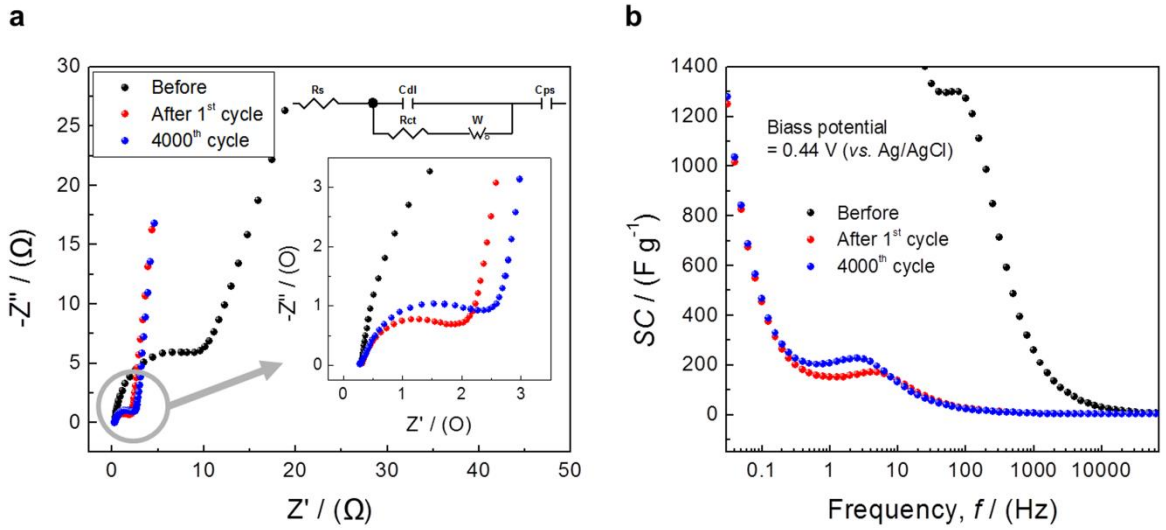

Figure S13. Electrochemical impedance spectroscopy (EIS) analysis. a, The complex-plane impedance plots (Nyquist plots; imaginary part, *Z*'' *versus* real part, *Z*') of the RT-Co_3O_4 electrode before and after 4,000 cycles. The insets show the enlarged Nyquist plot in the high-frequency region (the lower inset) and the equivalent circuit for the EIS spectra (the upper inset). **b**, Frequency-dependent specific capacitance values of the RT-Co_3O_4 electrode, calculated from impedance measurement. The EIS measurements were carried out by imposing a sinusoidal alternating voltage frequency of 100 kHz to 10 mHz at the open circuit voltage, an alternating current (AC) amplitude of 5 mV, and a constant direct current (DC) bias potential of 0.44 V (*vs.* Ag/AgCl) under the same conditions: a beaker-type three-electrode system with an aqueous electrolyte solution (3 M KOH) at room temperature.

Electrochemical impedance spectroscopy (EIS) analysis

As shown in Fig. R2-8a, it is seen that all EIS curves are similar in shape, composed of one depressed arc (partial semi-circle) in the high-frequency regions and an inclined line (straight slopping line along the imaginary axis) in the low-frequency regions with the transition between the two regions being called the "knee frequency". Two major characteristic features observed in the high and low frequency regions are attributed to various resistance phenomena during different interfacial processes in Faradaic reactions in a specific operating range. Such an EIS pattern can be explained by an equivalent circuit shown in the lower inset of Fig. 8a, which is proposed to fit the impedance data based on a Randles equivalent circuit, as proposed in previous reports[R5, R6, 44], where R_s and R_{ct} are the internal resistance and Faradaic interfacial charge-transfer resistance, respectively. C_{dl} and C_{ps} represent the double-layer capacitance and pseudo-capacitance, respectively. The interfacial diffusive resistance (Warburg impedance) in the process has been designated as "W". It is known that the equivalent series resistance (ESR), R_s, which is a combination of the ionic resistance of the electrolyte, intrinsic resistance of the active materials, and contact resistance at the active material-current collector interface, is an important parameter of the supercapacitor measured in the high-frequency region, where the impedance curve intercepts on the real axis. The higher ESR value indicates the lower electrical conductivity of the sample and vice versa. With the demonstrated parameters in the equivalent circuit, the R_s values of the RT-Co_3O_4 electrode are (0.27 Ω) and (0.30 d Ω) before and after 4,000 cycles, respectively, and is 0.28 Ω after the first cycle. It can be seen that the ESR values in the Nyquist plot of the Co_3O_4 electrode are very small and remain almost same before and after long-term charge/discharge cycling. This observation suggests very high organizational durability with good electrical conductivity as well as electrochemical stability of the porous-Co_3O_4 superstructure even after long charge-discharge cycles at high current densities and significant feasibility of redox

reactions even after the long-term charge-discharge process. The impedance behavior in the high frequency region also involves contributing resistance from the Faradaic redox process, named charge-transfer resistance (R_{ct}), which results from the diffusion of electrons and can be calculated from the diameter of the semi-circle in the high-frequency region. Such charge-transfer resistance is directly related to the surface properties of the porous electrode, that is, electroactive surface area (the combination of electrolyte accessible area and electrical conductivity) of the electrode materials. After 4,000 cycles, the R_{ct} value, about 1.39 Ω, is lower than the value (8.80 Ω) before the charge/discharge cycle. In particular, since the first cycle that leads to surface activation of the RT-Co_3O_4 electrode is tested, the small R_{ct} value remained almost the same until 4,000 cycles. This result may be due to the hierarchical formation of abundant meso-/macropores in RT-Co_3O_4 that can improve the diffusivity of the OH^- ions in the pore, which in turn, reduces the charge-transfer resistance without any appreciable structural change during high rate cycling, thereby leading to excellent pseudo-capacitive performance. In addition, the linear parts of the Nyquist plot in the lower frequency range correspond to the Warburg impedance, W, which is illustrated as the diffusive resistance of the electrolyte into the interior of the electrode pores and OH^- ion diffusion into the host materials (active sites). All profiles showed higher angles than 45 °, indicating the suitability as electrode materials for supercapacitors. In particular, the profile after the charge/discharge test for 4,000 cycles almost tended to a vertical asymptote along the imaginary line axis, indicating the good electrochemical capacitance of the porous-Co_3O_4 superstructures in the KOH aqueous electrolyte.

For a more informative representation, we converted the measured impedance data into specific capacitance as a function of frequency by using the following equation [R5, R6, 44]:

$$C_s = \frac{1}{2\pi f Z''} \quad (2)$$

where, Z'' is the imaginary part of the impedance and *f* is the measurement frequency. As shown in Fig. R2-8b, before the charge/discharge cycles and after 4,000 cycles, the specific capacitance values of the RT-Co_3O_4 electrode decreased considerably with increasing frequency. For the frequency range of 0.01 – 0.1 Hz, the RT-Co_3O_4 electrode shows maximum specific capacitance. This is due to the fact that the OH^- ions easily penetrate the pores of the RT-Co_3O_4 material with flower-like morphology and are electrochemically more accessible over a reasonable frequency range measured for the electrode. Besides, the relatively higher frequencies (1.0 – 10 Hz), it manifests a good frequency response with high specific capacitance after long-term charge/discharge cycles, even though the charge-transfer resistance is slightly increases. This suggests that the porous-Co_3O_4 superstructures with flower-like morphology are favorable and suitable for designing a supercapacitor electrode, and this trend is in agreement with the resistances observed for the RT-Co_3O_4 electrode in the impedance plots before and after galvanostatic charge/discharge cycling for 4,000 cycles.

References

R5. Wei, T. Y., Chen, C. H., Chang, K. H., Lu, S. Y. & Hu, C. C. *et al.* Cobalt oxide aerogels of ideal supercapacitive properties with an epoxide synthetic route. *Chem. Mater.* **21,** 3228-3233 (2009).

R6. Hsu, Y. k., Chen, Y. C., Lin, Y. G., Chen, L. C. & Chen, K. H. *et al.* Reversible phase transformation of MnO2 nanosheets in an electrochemical capacitor investigated by *in situ* Raman spectroscopy. *Chem. Commun.* **47,** 1252-1254 (2011).

44. Meher, S. K. & Rao, G. R. Ultralayered Co_3O_4 for high-performance supercapacitor applications. *J. Phys. Chem. C* **115,** 15646-15654 (2011).

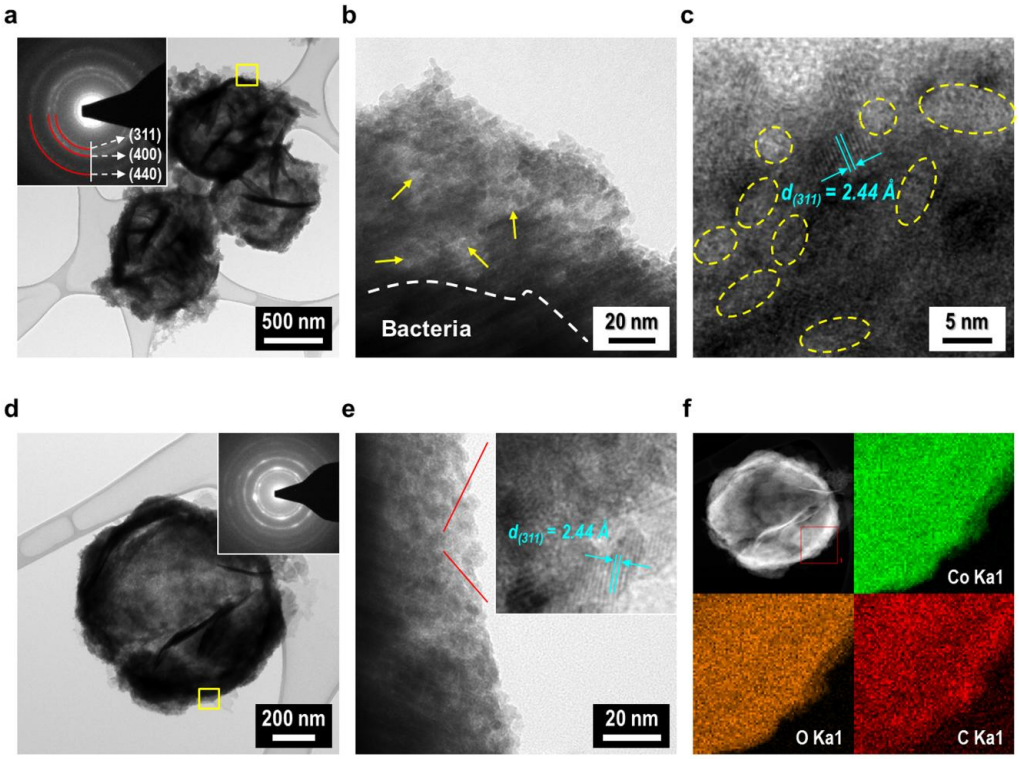

Figure S14. The structural stability of RT-Co_3O_4 electrode after charge/discharge for 4,000 cycles. a - c, The representative TEM and HR-TEM images of RT-Co_3O_4 after long-term cycling test. Low- (**a**) and high-magnification micrographs (**b**). The inset of (**a**) shows SAED pattern that is consistent with Co_3O_4 phase (JCPDS card #42-1467). **c**, HR-TEM image. Both the images of (**b**) and (**c**) were taken from the open-square zone of (**a**). The arrows and dashed-line circles in (**b**) and (**c**), respectively, reveal the porous regions. **d**, An individual TEM image of RT-Co_3O_4 after charge/discharge of 4,000 cycles. The inset is SAED pattern corresponding to the individual RT-Co_3O_4. **e**, The enlarged TEM image taken from the open-square zone of (**d**) and HR-TEM image (inset). **f**, The HAADF STEM image and the EDS elemental mapping analyses taken from the open-square zone (red line) in the HAADF STEM image.

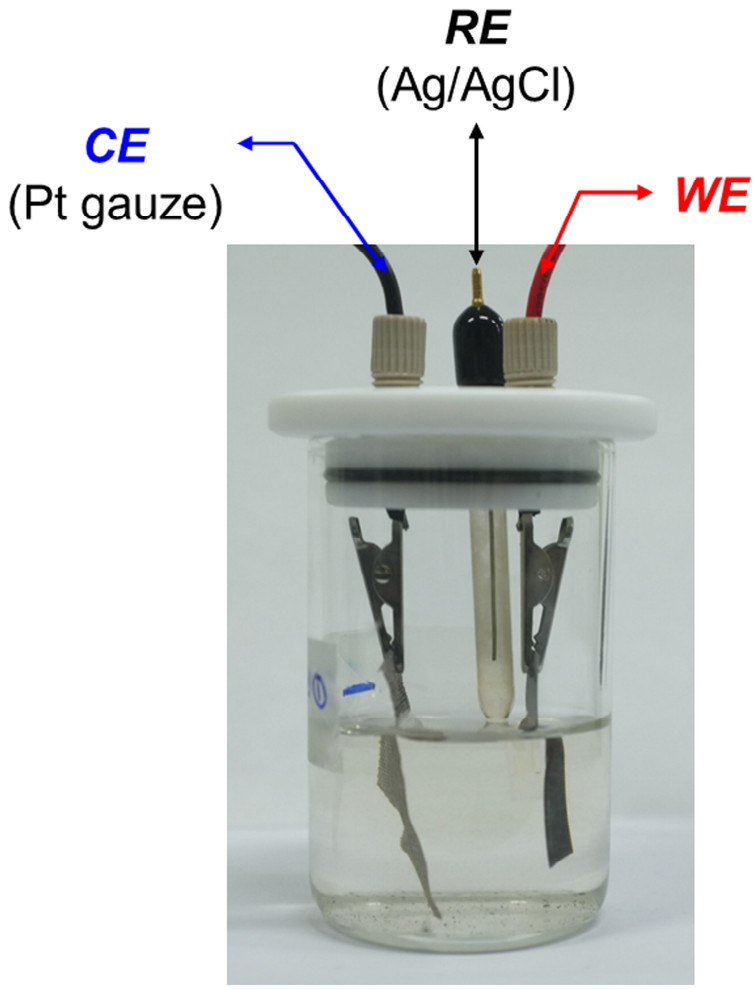

Figure S15. Digital photograph of the three-electrode system produced with 3 M KOH electrolyte. The photograph was taken after the 4,000-cycles galvanostatic charge-discharge test performed at a current density of 2 A g^{-1}. No change in the electrolyte was observed during the measurement of the cycling performance over the 4,000 cycles.

Table S1. A comparison of the specific capacitance *vs.* current density of the RT-Co_3O_4-microsphere-based electrode produced in this study with those of other electrodes previously reported in the literature. The values listed in the table take into account mass loading of the electrode active materials.

	Calculated specific capacitance, *SC*					References			
	Active material (mg cm^{-2})	Current density (A g^{-1})	(mA cm^{-2})	SC_{mass} (F g^{-1})	SC_{area} (F cm^{-2})	Active material (mg cm^{-2})	Current density or Scan rate	*SC*	Ref.
Total mass (Loading mass)	9.51	0.5	4.755	226	2.15	1	8 A g^{-1}	548 F g^{-1} (0.548 F cm^{-2})	[44]
		1	9.51	219	2.08	0.4	25 mV s^{-1}	719 F g^{-1} (0.288 F cm^{-2})	[41]
		2	19.02	214	2.04	0.5	2 A g^{-1}	358 F g^{-1} (0.179 F cm^{-2})	[27]
		5	47.55	163	1.55	1.4	10 mV s^{-1}	1090 F g^{-1} (1.526 F cm^{-2})	[21]
		10	95.1	106	1.01	0.8	2 A g^{-1}	454 F g^{-1} (0.363 F cm^{-2})	[R7]
		15	142.65	64	0.61	2.1	2 A g^{-1}	853 F g^{-1} (1.791 F cm^{-2})	[R8]
		20	190.2	36	0.34				
[a] RT-Co_3O_4	2.98	1.63		737		0.9	2 A g^{-1}	443 F g^{-1} (0.398 F cm^{-2})	[R9]
		3.26		712		1.8	2 A g^{-1}	325 F g^{-1} (0.585 F cm^{-2})	[R10]
		6.51		697		2	3 mV s^{-1}	102 F g^{-1} (0.204 F cm^{-2})	[R11]
		16.3		530		12.6	0.1 A g^{-1}	574 F g^{-1} (7.23 F cm^{-2})	[R12]
		32.6		345		3	1 A g^{-1}	291 F g^{-1} (0.873 F cm^{-2})	[R13]
		48.9		207					
		65.1		118		1	25 mV s^{-1}	623 F g^{-1}	[24]

[a] RT-Co_3O_4: an actual weight of the active material, Co_3O_4 except for the bacterial mass.

References

21. Wang, H. *et al.* Supercapacitive properties of hydrothermally synthesized Co_3O_4 nanostructures. *J. Phys. Chem. C* **115,** 17599-17605 (2011).

24. Wei, T. Y. *et al.* Cobalt oxide aerogels of ideal supercapacitive properties prepared with

an epoxide synthetic route. *Chem. Mater.* **21,** 3228-3233 (2009).

27. Xia, X. H. *et al.* Mesoporous Co_3O_4 monolayer hollow-sphere array as electrochemical pseudocapacitor material. *Chem. Commun.* **47,** 5786-5788 (2011).

44. Meher, S. K. & Rao, G. R. Ultralayered Co_3O_4 for high-performance supercapacitor applications. *J. Phys. Chem. C* **115,** 15646-15654 (2011).

41. Wei, T. Y. *et al.* A cost-effective supercapacitor material of ultrahigh specific capacitances: spinel nickel cobaltite aerogels from an epoxide-driven sol–gel process. *Adv. Mater.* **22,** 347-351 (2010).

R7. Duan, B. R. & Cao, Q. Hierarchically porous Co_3O_4 film prepared by hydrothermal synthesis method based on colloidal crystal template for supercapacitor application. *Electrochim. Acta* **64,** 154-161 (2012).

R8. Xia, X. *et al.* High-quality metal oxide core/shell nanowire arrays on conductive substrates for electrochemical energy storage. *ACS Nano* **6,** 5531-5538 (2012).

R9. Yuan, Y. F. *et al.* Hierarchically porous Co_3O_4 film with mesoporous walls prepared via liquid crystalline template for supercapacitor application. *Electrochem. Commun.* **13,** 1123-1126 (2011).

R10. Wu, J. B. *et al.* Pseudocapacitive properties of electrodeposited porous nanowall Co_3O_4 film. *Electrochim. Acta* **56,** 7163-7170 (2011).

R11. Wang, L. *et al.* Preparation and electrochemical properties of mesoporous Co_3O_4 crater-like microspheres as supercapacitor electrode materials. *Curr. Appl. Phys.* **10,** 1422-1426 (2010).

R12. Xu, J. *et al.* Preparation and electrochemical capacitance of cobalt oxide (Co_3O_4) nanotubes as supercapacitor material. *Electrochim. Acta* **56,** 732-736 (2010).

R13. Wang, H. W. *et al.* Preparation of reduced graphene oxide/cobalt oxide composites and their enhanced capacitive behaviors by homogeneous incorporation of reduced graphene

oxide sheets in cobalt oxide matrix. *Mater. Chem. Phys.* **130,** 672-679 (2011).